Supporting Materials – Methods, Tables and Figures

Populations of *in silico* myocytes and tissues reveal synergy of multi-atrial-predominant-K^+ current block in atrial fibrillation

Haibo Ni,[1] Alex Fogli Iseppe,[1] Wayne R. Giles,[2] Sanjiv M. Narayan,[3] Henggui Zhang,[4] Andrew G. Edwards,[1] Stefano Morotti,[1] and Eleonora Grandi[1*]

[1]Department of Pharmacology, University of California, Davis, CA, USA.

[2]Faculties of Kinesiology and Medicine, University of Calgary, Calgary, Canada.

[3]Division of Cardiology, Cardiovascular Institute, Stanford University, Stanford, CA, USA.

[4]Biological Physics Group, School of Physics & Astronomy, The University of Manchester, Manchester, UK.

***Correspondence** ele.grandi@gmail.com

Supporting Methods

Overall study design

We developed a novel Quantitative Systems Pharmacology framework (see schematic below) to simulate and quantitatively assess synergistic anti-AF effects of multi-K^+ current block in human AF. **1)** We constructed GB and CZ populations of models, which were calibrated to experimental data. **2)** We performed sensitivity analysis of APD measured from the populations to predict i) effects of blocking the currents of interest on APD, and ii) RD of such APD change. **3)** Simulations of single current block using the physiological model populations were conducted to confirm the predictions from *Step 2*. **4)** We derived quantification of repolarization reserve (RR) using the simulated single current block (in *Step 3*), and applied sensitivity analysis of RR to uncover the interactions (synergisms or antagonism) among modulations of K^+-current block. **5)** Simulations of multiple K^+-current block using physiological model populations were performed to confirm the predicted interactions from *Step 4*. **6)** We performed additional simulations using atrial tissue populations to examine the effects of multi-current block in coupled tissue.

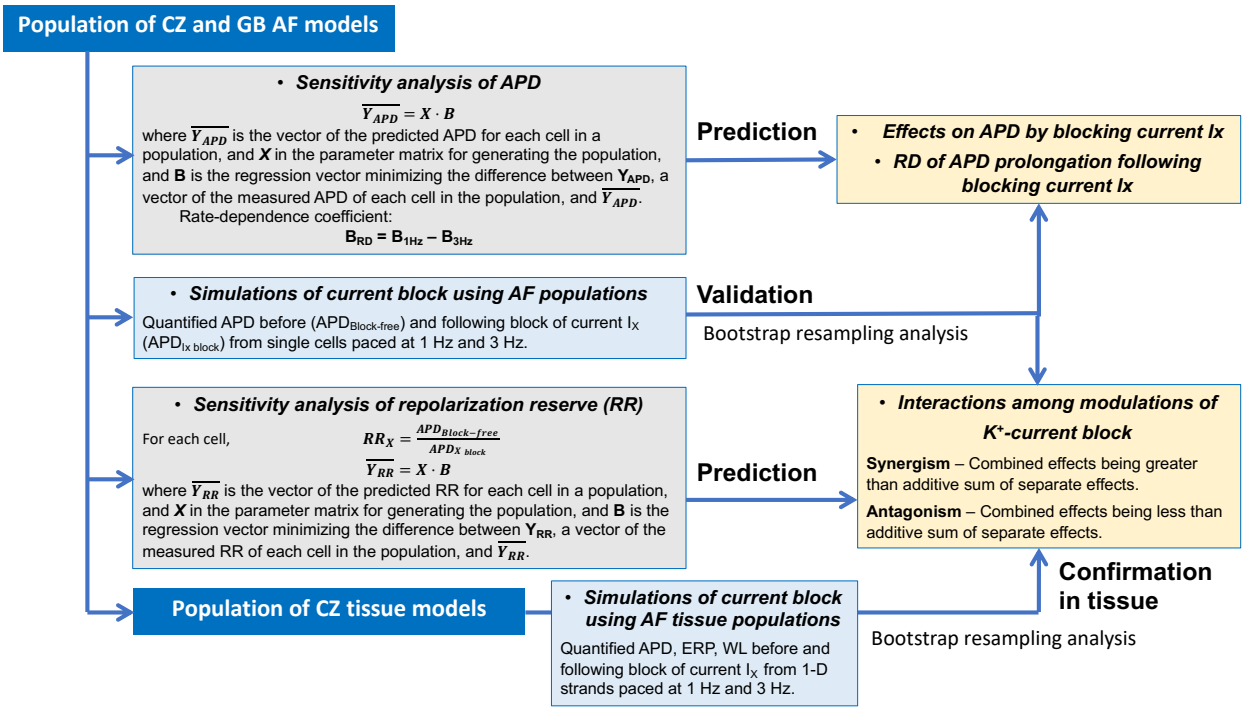

Workflow for constructing populations

The workflow for generating our nSR and AF populations of models is shown as follows.

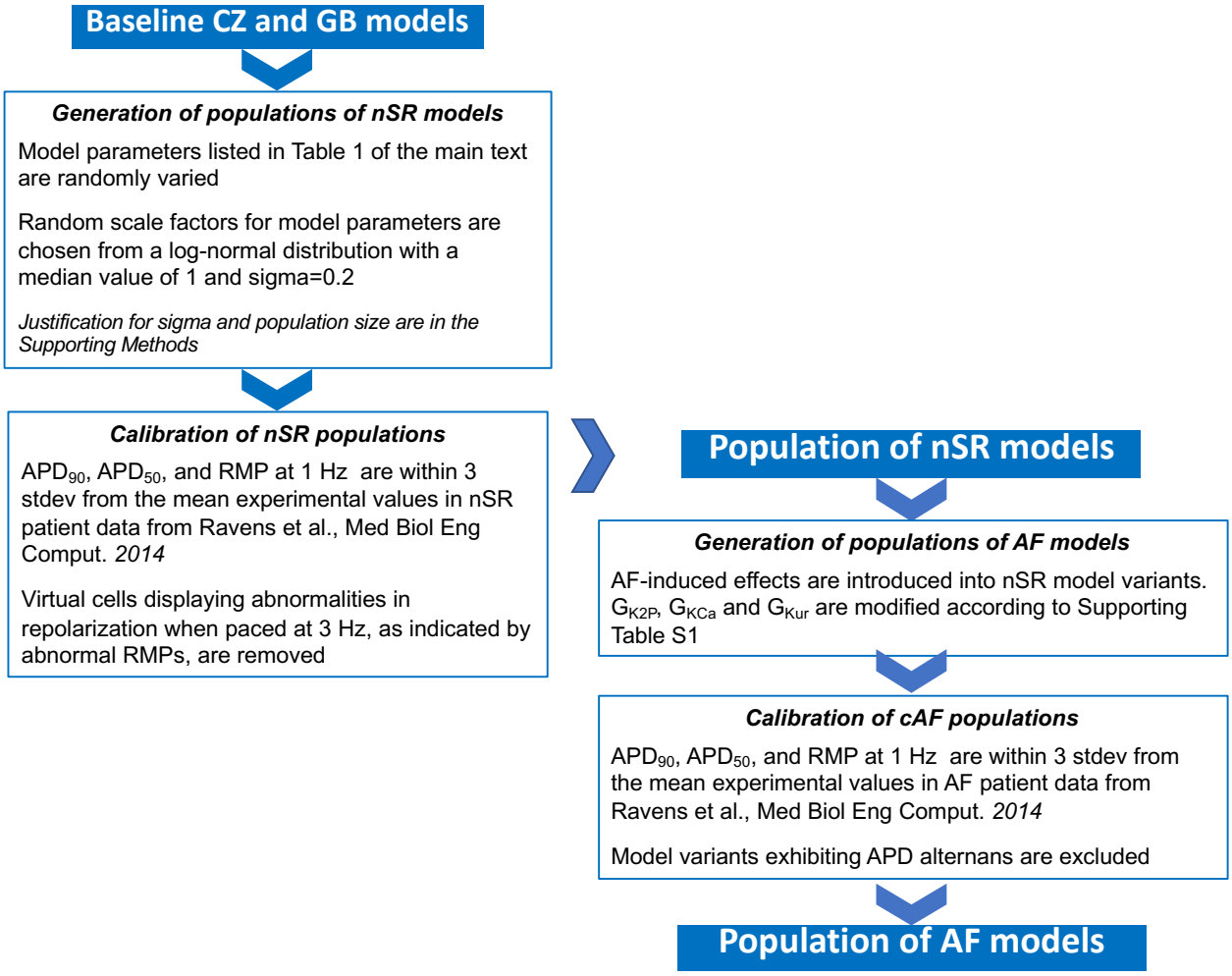

Model parameters for generating populations

Populations of models are generated as previously described (Sobie, 2009) by randomly perturbing transmembrane ionic current and transporter parameters of CZ and GB baseline models. The CZ and GB models possess different numbers of transmembrane ionic currents (**Table 1** of the main text). The total number of perturbed parameters was 15 and 16 for CZ and GB model, respectively. In the CZ model, the late component of Na^+ current was modeled with the parameter G_{NaL}, independently from the fast-inactivating component of the Na^+ current. In contrast, in the GB model Na^+ currents were described using a Markov formulation as in (Morotti et al., 2016), and thus G_{Na} depicts the conductance of both fast-inactivating and late components of the Na^+ current. Further, two currents are present in GB but not CZ model, the background (I_{ClB}) and Ca^{2+} activated (I_{ClCa}) Cl^- currents.

Population size

We take three factors into consideration when determining the size of a model population. 1) We want to ensure convergence of the regression model, i.e., the sensitivity coefficients are not affected by an increase in the population size. To do so, we required results from randomly resampled subsets of populations to converge to those from the whole population, as we have done in a previous study (Ellinwood et al., 2017a). 2) We expect some model variants will be excluded at the experimental calibration stage, thus reducing the population size available for data analysis. 3) The computational cost is a concern due to the substantial computational time required for performing population-of-models.

We determined that 600 variants were sufficient for convergence of the sensitivity coefficients for both CZ and GB nSR model populations, but because a larger number of CZ virtual cells had to be excluded upon calibration and subsequent analyses, we doubled the initial size of the CZ model population to 1200 variants. As per the criteria of model calibration described in Methods, 180 and 4 model variants were excluded from the CZ and GB populations, resulting in 1020 and 596 for the CZ and GB nSR populations, respectively. With the introduction of 12 AF subpopulations, generated by superimposing AF-induced ionic changes on each accepted nSR model variant, 12440 CZ and 7152 GB AF model variants were created. Calibration of the AF populations reduced the total number to 10408 and 7063, respectively. For the purpose of quantifying APD changes, we excluded the model variants exhibiting APD_{90} alternans, leading to a total number of model variants for data analysis of 8933 and 7050 for the CZ and GB models, respectively.

Simulation protocols

In our single cell simulations, we paced each model variant at 1 or 3 Hz to steady state and recorded the last two APs for biomarker analysis. We define that steady-state is reached when 1) variation in APD_{90} from the last 5 beats is less than time step, and 2) the intracellular Na^+ concentration does not drift (beat-to-beat change < 0.001 mM). Given this definition, constant pacing protocols lasting 500 sec ensured steady state was reached in both nSR and AF simulations with both CZ and GB models with and without K^+-channel block (Time-matched control). Effects of channel block were quantified by pacing each model variant at 1- and 3-Hz for 500 s from baseline steady-state conditions and collecting the last two AP cycles for data analysis.

The 1D models consisted of 200 nodes spaced evenly by 0.3 mm. Electrical coupling in tissue was described using the monodomain equation and solved as described previously (Ni et

al., 2017). Fifteen nodes at the left end of the strand were paced at 1 or 3 Hz to quantify in-tissue APD, effective refractory period (ERP), CV and wavelength (WL). We recorded APD and AP upstroke time for nodes number 100 and 180 to compute CV. WL was then obtained as the product of APD and CV. ERP was defined as the longest S1-S2 coupling that failed to capture the whole atrial strand. In these simulations, to reduce computational cost for reaching steady-state, we first obtained steady-state model state variables from single cell simulations in each condition as described above; next, we applied uniformly these state variables to the 1D strand model, which was subjected to a train of 100 beats at constant (S1) pacing. The last two beats were recorded for APD and CV analysis. Also, at the end of the S1 simulation, state-variables for all nodes in the strand model were saved to a binary file, thus facilitating and accelerating the following measurement of ERP by repeatedly varying the delay in applying the S2 stimulus.

Comparing sensitivity coefficients

We applied sensitivity analysis using the multivariable linear regression method as detailed in previous studies (Sobie, 2009; Sarkar and Sobie, 2011; Cummins et al., 2014). As described in the previous studies, sensitivity coefficients were normalized to the ratio of standard deviations of model output to parameter variabilities (i.e., $\sigma_{output}/\sigma_{parameter}$) for each simulation condition. To enable comparison of sensitivity coefficients calculated under different conditions (e.g., pacing rates or various current blocking conditions), an additional scaling for the coefficients is necessary (Cummins et al., 2014) so that the values are normalized to the same 'unit' ($\sigma_{output}/\sigma_{parameter}$). For example, to make direct comparison of sensitivity coefficients at 1 ($\mathbf{B_1}$) vs 3 Hz ($\mathbf{B_3}$) and calculate $\mathbf{B}_{RD}$, $\mathbf{B_3}$ was multiplied by $\sigma_{output,3Hz}/\sigma_{output,1Hz}$, given that $\sigma_{parameter,1Hz} = \sigma_{parameter,3Hz}$. Additionally, because parameter variability was much greater for G_{Kur}, G_{KCa} and G_{K2P} for the GB and CZ aggregate AF model population encompassing 12 AF-subpopulations (**Supporting Table S1**), when comparing sensitivity coefficients of the aggregate AF population vs. individual subpopulation, we scaled the coefficients of each subpopulation so that all values are normalized to $\sigma_{output,aggregate\ population}/\sigma_{parameter}$.

Software, numerical methods, and data analysis

The CZ model and 1D strand model were both implemented in C++. The ODEs were solved using a combination of the Forward Euler method and the Rush-Larsen scheme (Rush and Larsen, 1978), as implemented in previous studies (Courtemanche et al., 1998; Colman et al., 2017; Ni et al., 2017). The monodomain equation describing the cell-to-cell electrical coupling was solved

using a finite-difference PDE solver based on the explicit Forward Euler scheme and Strang splitting scheme (Sundnes et al., 2005).

The GB model was implemented in MATLAB 2018a (The MathWorks, Natick, MA, USA) using the stiff ordinary differential equation solver ode15s as in our previous studies (Grandi et al., 2011; Morotti et al., 2016; Ellinwood et al., 2017a, 2017b; Morotti and Grandi, 2017).

All simulations and data analyses were performed on a desktop server: HP 240, Intel(R) Core(TM) i7-7700K @ 4.20GHz 4CPUs (8 threads) + 32GB; and a computing cluster with Intel(R) Xeon(R) CPU E5-2690 v4 @ 2.60GHz 28 CPUs (56 threads) + 132GB. Simulations of the AF populations necessitated significant amount of computational time: approximately 10 days of running time was required to complete the single cell simulations of the 12 subpopulations of the CZ model under both baseline and 50% current blockade conditions; two weeks were needed to finish the GB population simulations under the same condition. Further, tissue simulations of a single AF subpopulation (CZ model) took approximately 5 days.

We used the non-parametric bootstrap method to characterize the RD of APD (and other tissue-level biomarkers) changes and interactions of multiple channel blockades. Specifically, RD of APD change was deemed positive if the lower limit of the confidence interval (CI) for the median of $\Delta APD_{3Hz} - \Delta APD_{1Hz}$ is > 0, and negative if the upper limit of CI is < 0. Potential interactions were assessed by comparing changes due to combined block and the sum of the effects of each individual current block. Using again APD as an example, the interaction between I_{K2P} and I_{Kur} block is calculated as

$$\mathrm{Interaction}_{\mathrm{K2P+Kur}} = \Delta\mathrm{APD}_{\mathrm{K2P+Kur\ block}} - (\Delta\mathrm{APD}_{\mathrm{K2P\ block}} + \Delta\mathrm{APD}_{\mathrm{Kur\ block}})$$

where for each current block, $\Delta\mathrm{APD}_{\mathrm{X\ block}} = \frac{\mathrm{APD}_{\mathrm{X\ block}} - \mathrm{APD}_{\mathrm{Block-free}}}{\mathrm{APD}_{\mathrm{Block-free}}} \times 100\ (\%)$. Hence, an interaction exists if the CI for the median $Interaction_{K2P+Kur}$ does not contain 0, and is deemed synergistic if the lower limit of CI is > 0 and antagonistic if the upper limit of CI is < 0.

The non-parametric bootstrap analyses were implemented in R (version 3.6.1, (R Core Team, 2019)) using packages *boot* (Davison and Hinkley, 1997; Canty and Ripley, 2019) and *simpleboot* (Peng, 2019) for interactions and RD, respectively. In both cases, a total of 10,000 bootstrapped samples were generated, and the median value was calculated, forming a resampling distribution for each biomarker of interest. CIs were obtained using the function *boot.ci* from the *boot* package with confidence levels set to 95% with Bonferroni-type correction for each group of data analysis (i.e., considering 7 comparisons for RD characterizations and 4 comparisons/combination-of-currents for interactions for each subpopulation).

Supporting Tables

Supporting Table S1. AF model subpopulations created with different combinations of AF-remodeling induced modulations on I_{Kur}, I_{KCa} and I_{K2P}.

AF subpopulation #		0	1	2	3	4	5	6	7	8	9	10	11
Fold-change due to AF-remodelling	G_{Kur}	0.5 [a]	0.5 [a]	0.5 [a]	0.5 [a]	0.5 [a]	0.5 [a]	1 [b]	1 [b]	1 [b]	1 [b]	1 [b]	1 [b]
	G_{KCa}	0.5 [c]	0.5 [c]	1	1	2 [d]	2 [d]	0.5 [c]	0.5 [c]	1	1	2 [d]	2 [d]
	G_{K2P}	1	3 [e]	1	3 [e]	1	3 [e]	1	3 [e]	1	3 [e]	1	3 [e]

[a] (Wagoner et al., 1997; Caballero et al., 2010; Gonzalez de la Fuente et al., 2012).
[b] (Bosch et al., 1999; Grammer et al., 2000; Workman et al., 2001).
[c] (Skibsbye et al., 2014)
[d] (Ozgen et al., 2007; Qi et al., 2014)
[e] (Schmidt et al., 2015, 2017)

Supporting Table S2. Summary of action potential duration (APD) and resting membrane potential (RMP) of the simulated atrial populations in nSR and AF conditions. [a]

		CZ Model		GB Model		Exp. (Ravens et al. 2014)	
		APD_{90} (ms)	RMP (mV)	APD_{90} (ms)	RMP (mV)	APD_{90} (ms)	RMP (mV)
SR	1 Hz	244.3 ± 22.1	-76.0 ± 2.4	262.5 ± 26.3	-74.3 ± 2.3	317.4 ± 43.2	-74.0 ± 4.0
	3 Hz	185.2 ± 34.2	-75.9 ± 3.4	235.1 ± 19.6	-73.0 ± 2.7		
AF	1 Hz	169.1 ± 31.3	-81.6 ± 1.0	193.1 ± 20.0	-78.1 ± 1.3	217.5 ± 35.7	-76.9 ± 3.6
	3 Hz	109.0 ± 24.3	-82.0 ± 1.1	177.8 ± 24.1	-78.5 ± 1.3		

[a] Values are presented in mean ± std.

Supporting Table S3. Summary of APD and RMP for each AF subpopulation with the CZ and GB models. [a]

AF Population Groups		CZ Model		GB Model	
		1Hz	3Hz	1Hz	3Hz
APD_{90} (ms)	0	195.5 ± 29.9	130.3 ± 25.0	209.7 ± 18.3	207.2 ± 21.7
	1	161.4 ± 26.7	104.9 ± 19.8	185.8 ± 15.0	173.1 ± 17.2
	2	188.7 ± 28.1	126.1 ± 23.9	203.8 ± 17.2	198.9 ± 20.2
	3	157.7 ± 24.7	102.9 ± 19.0	181.3 ± 14.2	167.5 ± 16.1
	4	176.6 ± 25.6	118.4 ± 22.1	193.3 ± 15.7	184.4 ± 18.0
	5	151.1 ± 21.5	99.1 ± 17.8	173.2 ± 13.0	157.5 ± 14.4
	6	185.2 ± 32.7	114.4 ± 25.4	211.7 ± 17.5	195.9 ± 19.5
	7	153.0 ± 25.8	95.9 ± 17.8	190.0 ± 14.7	167.7 ± 15.8
	8	179.0 ± 30.5	111.2 ± 24.2	206.3 ± 16.6	188.8 ± 18.4
	9	150.0 ± 23.8	94.6 ± 17.0	185.7 ± 13.9	162.6 ± 14.8
	10	168.7 ± 27.0	105.9 ± 22.5	196.1 ± 15.2	175.9 ± 16.3
	11	144.6 ± 20.9	92.1 ± 16.0	177.7 ± 12.8	153.4 ± 13.3
APD_{50} (ms)	0	123.8 ± 26.4	67.1 ± 19.5	61.8 ± 10.5	105.5 ± 18.5
	1	93.7 ± 23.7	48.9 ± 14.6	50.4 ± 8.6	72.0 ± 13.4
	2	120.4 ± 25.3	65.6 ± 19.0	60.8 ± 10.1	99.1 ± 17.0
	3	92.5 ± 22.5	48.5 ± 14.3	49.8 ± 8.4	69.1 ± 12.2
	4	114.4 ± 23.3	62.9 ± 17.9	58.9 ± 9.5	88.7 ± 14.4
	5	90.1 ± 20.2	47.7 ± 13.7	48.7 ± 8.0	64.2 ± 10.6
	6	105.0 ± 28.5	49.5 ± 17.7	48.6 ± 8.9	87.5 ± 16.2
	7	78.3 ± 24.0	38.0 ± 12.1	40.9 ± 7.6	60.6 ± 11.5
	8	102.2 ± 27.2	48.8 ± 17.2	47.8 ± 8.6	82.1 ± 14.6
	9	77.6 ± 22.6	38.1 ± 11.8	40.5 ± 7.4	58.1 ± 10.5
	10	97.6 ± 24.7	47.5 ± 16.3	46.6 ± 8.0	73.6 ± 12.2
	11	75.9 ± 20.8	37.8 ± 11.4	39.7 ± 7.1	54.2 ± 8.9
RMP (mV)	0	-81.6 ± 1.1	-81.7 ± 1.2	-77.8 ± 1.3	-77.8 ± 1.5
	1	-81.7 ± 1.0	-82.1 ± 1.1	-78.1 ± 1.2	-78.6 ± 1.2
	2	-81.6 ± 1.1	-81.8 ± 1.2	-77.9 ± 1.3	-78.1 ± 1.4
	3	-81.7 ± 1.0	-82.1 ± 1.0	-78.2 ± 1.2	-78.8 ± 1.2
	4	-81.7 ± 1.0	-82.0 ± 1.1	-77.9 ± 1.3	-78.4 ± 1.3
	5	-81.7 ± 1.0	-82.2 ± 1.0	-78.2 ± 1.2	-79.0 ± 1.1
	6	-81.6 ± 1.1	-81.9 ± 1.2	-78.0 ± 1.3	-78.2 ± 1.4
	7	-81.6 ± 1.0	-82.0 ± 1.0	-78.2 ± 1.2	-78.8 ± 1.2
	8	-81.6 ± 1.1	-82.0 ± 1.1	-78.0 ± 1.3	-78.3 ± 1.3
	9	-81.6 ± 1.0	-82.1 ± 1.0	-78.3 ± 1.2	-78.9 ± 1.2
	10	-81.6 ± 1.0	-82.1 ± 1.1	-78.0 ± 1.3	-78.6 ± 1.2
	11	-81.6 ± 1.0	-82.2 ± 1.0	-78.3 ± 1.2	-79.1 ± 1.1

[a] Values are quoted in mean ± std.

Supporting Table S4. APD_{90} changes due to 50% of mono- or multi- K^+ currents in the CZ and GB AF-populations. [a]

50% block of			I_{K2P}	I_{KCa}	I_{Kur}	$I_{K2P}+I_{KCa}$	$I_{K2P}+I_{Kur}$	$I_{KCa}+I_{Kur}$	$I_{K2P}+I_{KCa}+I_{Kur}$
ΔAPD_{90} (ms)	CZ Model	1Hz	19.4 ± 11.3	6.9 ± 4.8	11.3 ± 6.9	28.2 ± 11.0	28.9 ± 13.7	19.1 ± 7.1	38.4 ± 13.3
		3Hz	13.2 ± 7.0	3.6 ± 2.9	12.1 ± 6.0	18.0 ± 7.3	26.2 ± 9.7	16.8 ± 6.9	32.4 ± 9.7
	GB Model	1Hz	11.1 ± 5.0	5.7 ± 3.5	-1.8 ± 3.4	17.6 ± 5.8	10.6 ± 6.2	4.0 ± 5.2	17.3 ± 7.2
		3Hz	14.5 ± 6.5	7.1 ± 4.3	7.4 ± 3.5	23.0 ± 7.2	24.5 ± 6.7	15.1 ± 6.3	33.7 ± 7.6
ΔAPD_{90} (%)	CZ Model	1Hz	12.5 ± 8.7	4.1 ± 2.8	7.3 ± 5.1	17.8 ± 9.0	18.7 ± 11.3	12.0 ± 5.8	24.5 ± 11.8
		3Hz	12.9 ± 7.5	3.4 ± 2.5	12.0 ± 7.0	17.5 ± 8.0	26.3 ± 12.5	16.5 ± 8.1	32.2 ± 13.4
	GB Model	1Hz	5.8 ± 2.7	3.0 ± 1.8	-1.0 ± 1.8	9.2 ± 3.3	5.6 ± 3.3	2.0 ± 2.7	9.0 ± 3.8
		3Hz	8.4 ± 4.0	4.0 ± 2.4	4.0 ± 1.6	13.2 ± 4.6	13.9 ± 3.9	8.4 ± 3.1	19.2 ± 4.5

[a] Values are presented in mean ± std. Both absolute and relative differences are given in this table.

Supporting Table S5. Summary of sensitivity coefficients describing influence of G_{K2P}, G_{KCa} and G_{Kur} on atrial repolarization reserve measured via blocking I_{K2P}, I_{KCa} or I_{Kur}, respectively. [a]

Pacing rate	Repolarization reserve via current blockade	Sensitivity coefficient					
		CZ model			GB model		
		G_{K2P}	G_{KCa}	G_{Kur}	G_{K2P}	G_{KCa}	G_{Kur}
1 Hz	I_{K2P}		**0.033**	**-0.092**		**0.035**	**0.067**
	I_{KCa}	**0.094**		**0.049**	**0.047**		0.019
	I_{Kur}	**-0.123**	0.026		**0.139**	0.013	
3 Hz	I_{K2P}		**0.031**	-0.014		**0.063**	**0.124**
	I_{KCa}	**0.096**		**0.085**	**0.086**		**0.040**
	I_{Kur}	-0.013	**0.035**		**0.200**	**0.032**	

[a] Coefficients are colored by sign and shown in bold text if magnitude greater than 0.03.

Supporting Table S6. Summary of simulated APD_{90}, wavelength (WL) and effective refractory period (ERP) in the 1D strand tissue models in AF conditions in the absence or presence of AF-remodeling on tissue electrical coupling. [a]

AF subpopulation		APD_{90} (ms)		WL (mm)		ERP (ms)		CV (m/s)	
		1 Hz	3 Hz	1 Hz	3 Hz	1 Hz	3 Hz	1 Hz	3 Hz
Control tissue coupling	1	167.1 ± 27.2	108.0 ± 22.1	104.5 ± 20.3	65.4 ± 15.6	182.6 ± 27.2	126.2 ± 22.2	0.624±0.054	0.603±0.054
	5	156.3 ± 21.7	102.2 ± 19.6	97.8 ± 16.9	61.8 ± 14.0	173.0 ± 21.9	120.3 ± 19.7	0.625±0.054	0.602±0.054
With 40% reduction in tissue coupling	1	169.0 ± 27.2	108.6 ± 22.3	77.6 ± 15.1	48.4 ± 11.7	182.9 ± 27.3	126.5 ± 22.3	0.461±0.042	0.444±0.041
	5	157.2 ± 21.7	102.8 ± 19.8	72.7 ± 12.6	45.7 ± 10.6	173.3 ± 21.9	120.5 ± 19.8	0.461±0.042	0.443±0.042

[a] Values are presented as mean ± std.

Supporting Figures

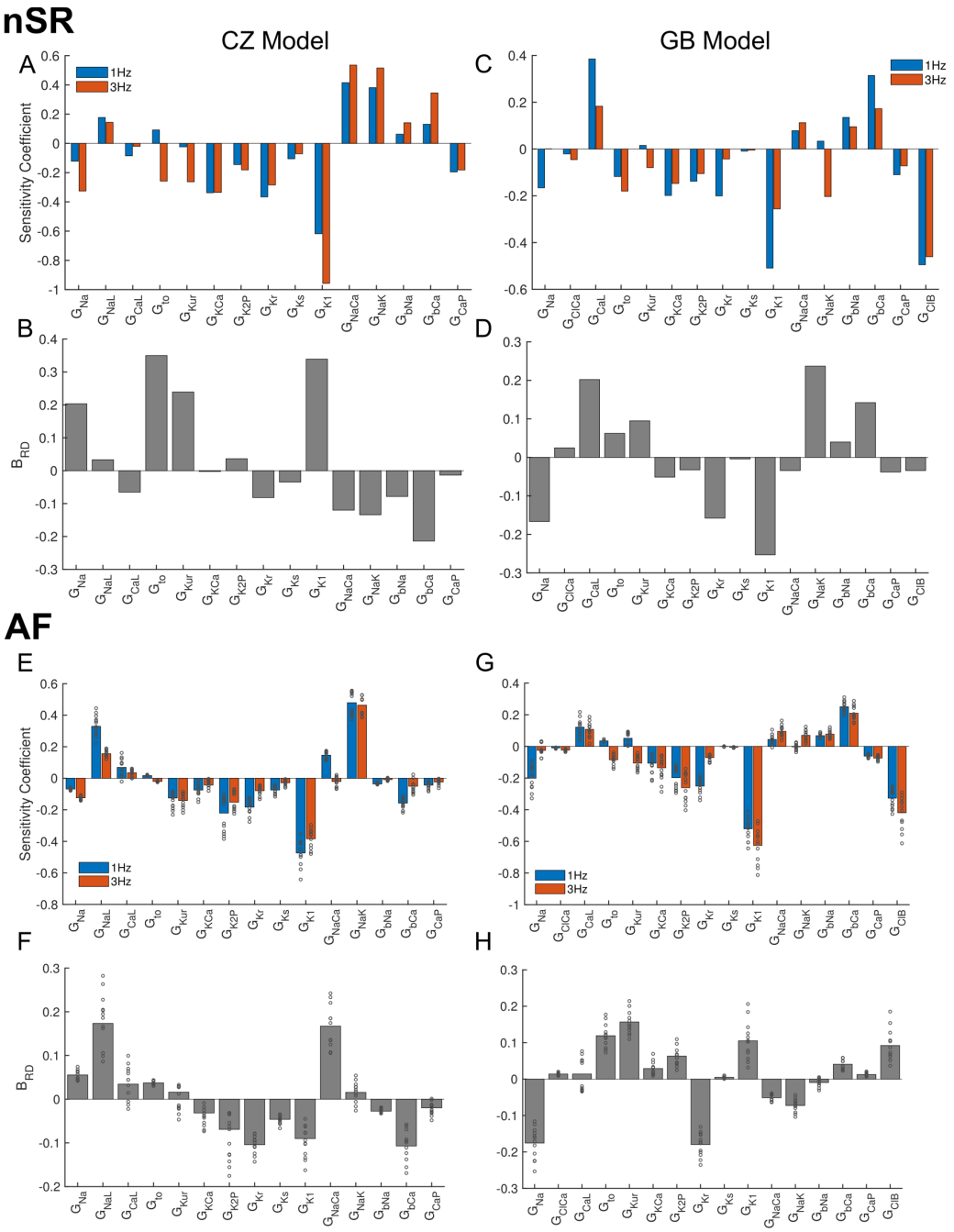

Supporting Figure S1. **Parameter sensitivity analysis of APD and rate-dependent APD modulation for the virtual atrial populations.** (A-D) nSR populations. (E-H) AF populations. (A,C,E,G) Sensitivity coefficients of APD to perturbations of transmembrane currents for myocytes paced at 1 Hz and 3 Hz. (B,D,F,H) APD rate-dependence coefficients (B_{RD}) for these transmembrane currents. Positive B_{RD} indicates inhibition of this current favors producing positive rate-dependence of APD prolongation, and vice versa. In (E-H), results for each AF subpopulation are plotted as open circles and those for the aggregate dataset are represented by bar plots.

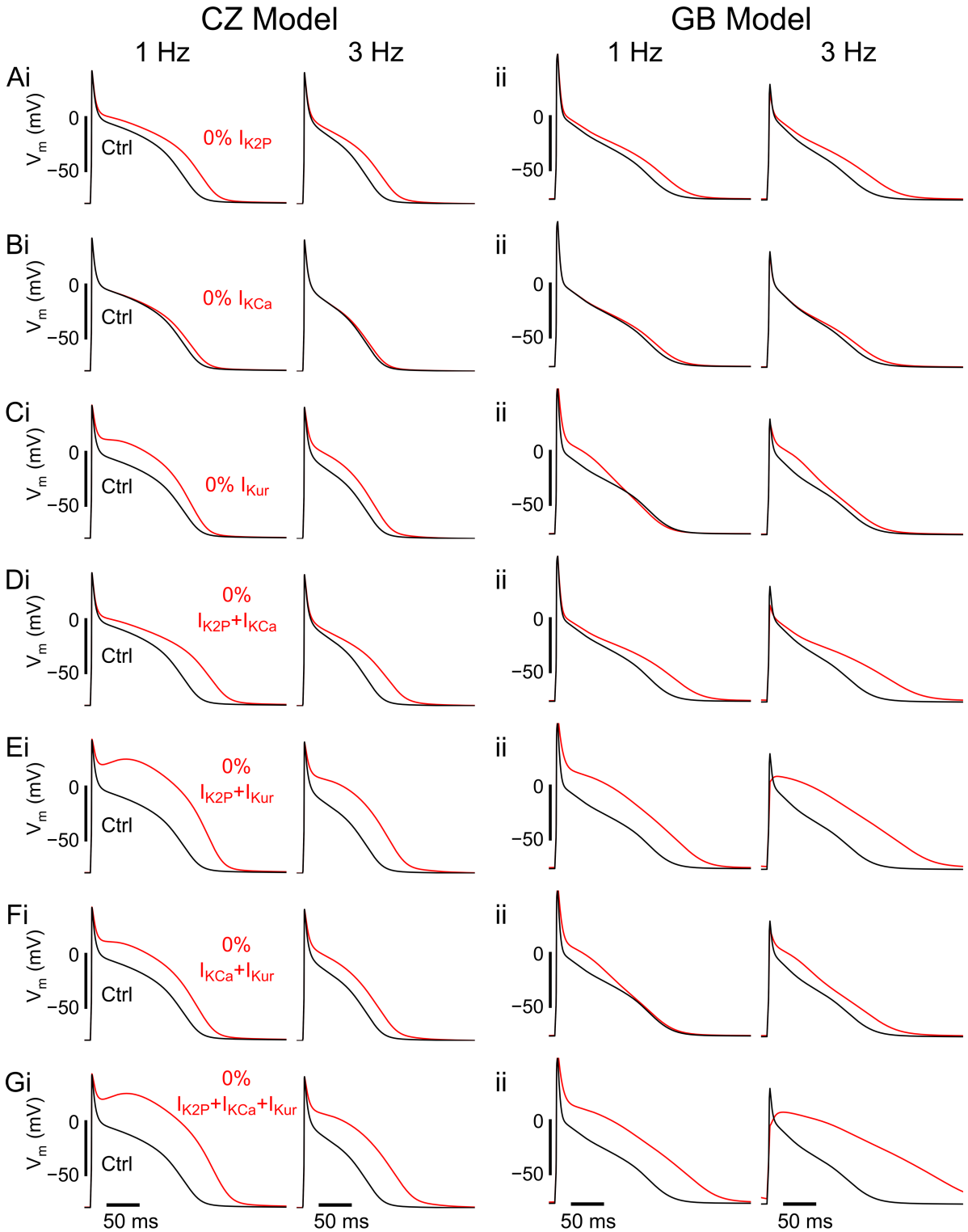

Supporting Figure S2. Example of AP modulations at 1 and 3 Hz by 100% block of (A) I_{K2P}, (B) I_{KCa}, (C) I_{Kur}, (D) I_{K2P}+I_{KCa}, (E) I_{K2P}+I_{Kur}, (F) I_{KCa}+I_{Kur} and (G) I_{K2P}+I_{KCa}+I_{Kur} from simulations with (left columns) CZ (subpopulation #5, variant #310) and (right columns) GB models (subpopulation #5, variant #287). Cells were chosen so that the block-free APD and ΔAPD of single-current block were close to the median values of the population shown in Fig. 4 of the main text.

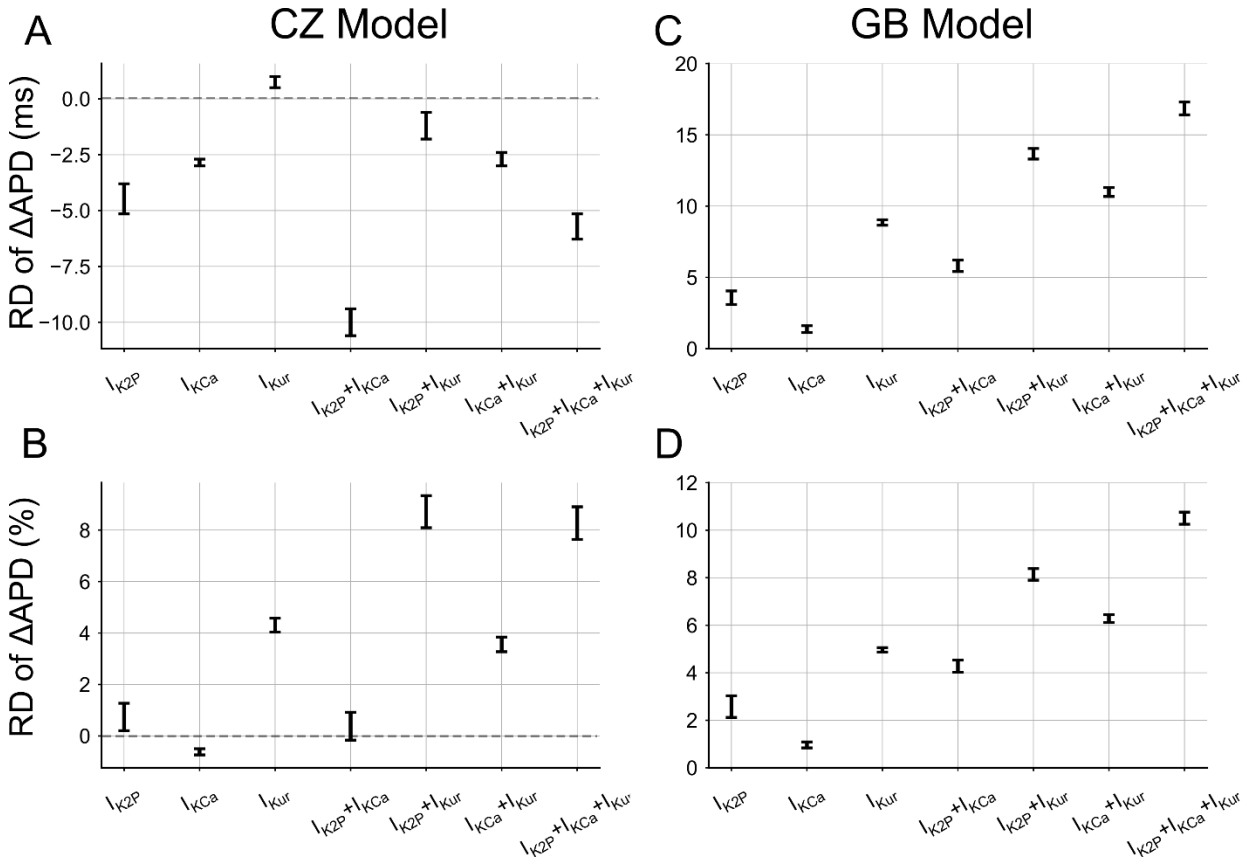

Supporting Figure S3. Confidence interval of rate-dependent changes in ΔAPD (3 Hz vs 1 Hz) shown in Figure 4 of the main text. RD of ΔAPD is defined as RD = ΔAPD_{3Hz} – ΔAPD_{1Hz}.

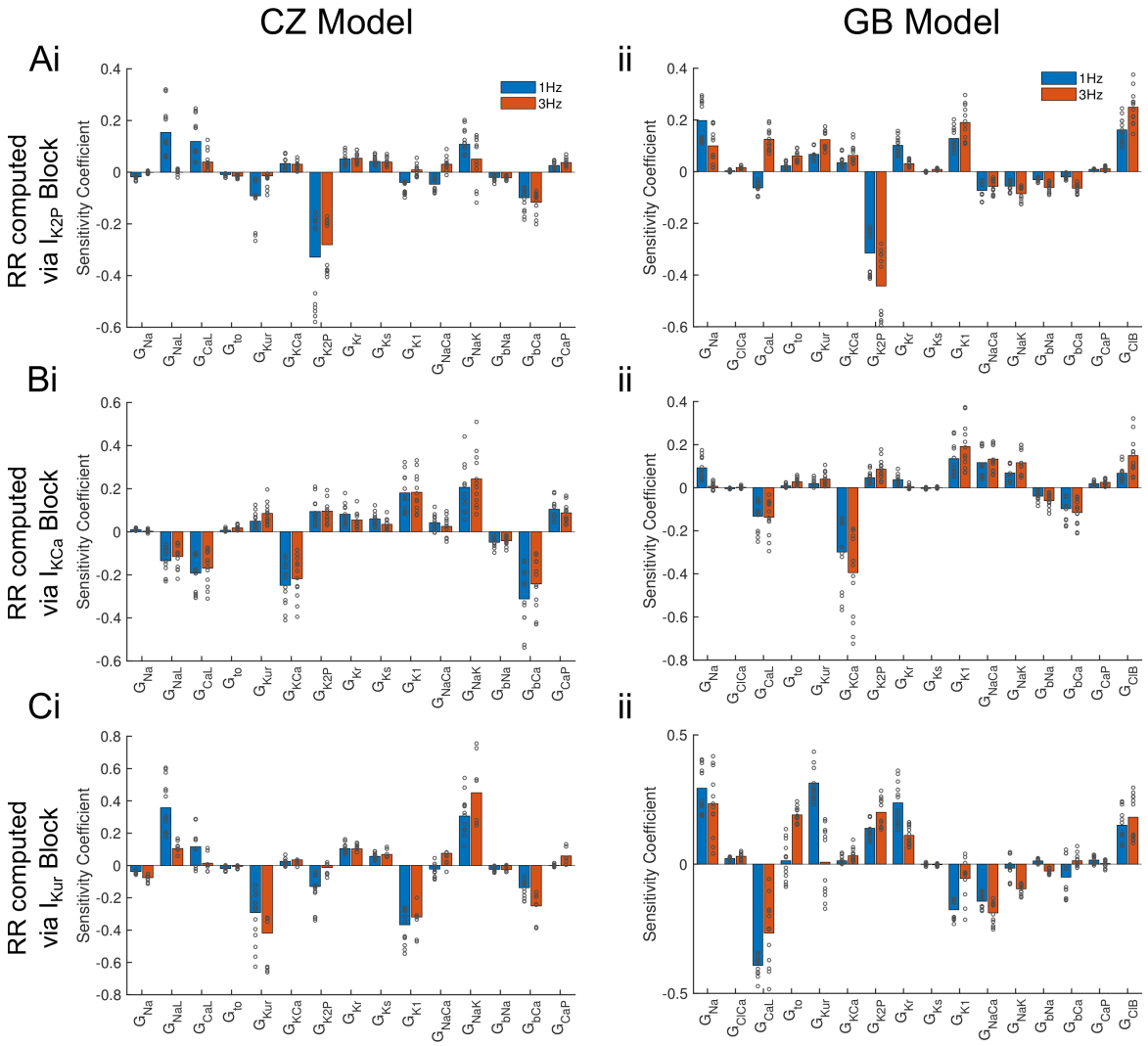

Supporting Figure S4. Parameter sensitivity of repolarization reserve.
(A-C) Sensitivity coefficients of repolarization reserve (RR) derived from the ratio between APD before and after 50% block of (A) I_{K2P}, (B) I_{KCa} and (C) I_{Kur}. Columns are sensitivity coefficients for the (i) CZ and (ii) GB populations. Results for each AF subpopulation are plotted with open circles and those for the aggregate AF dataset are shown in bar plots.

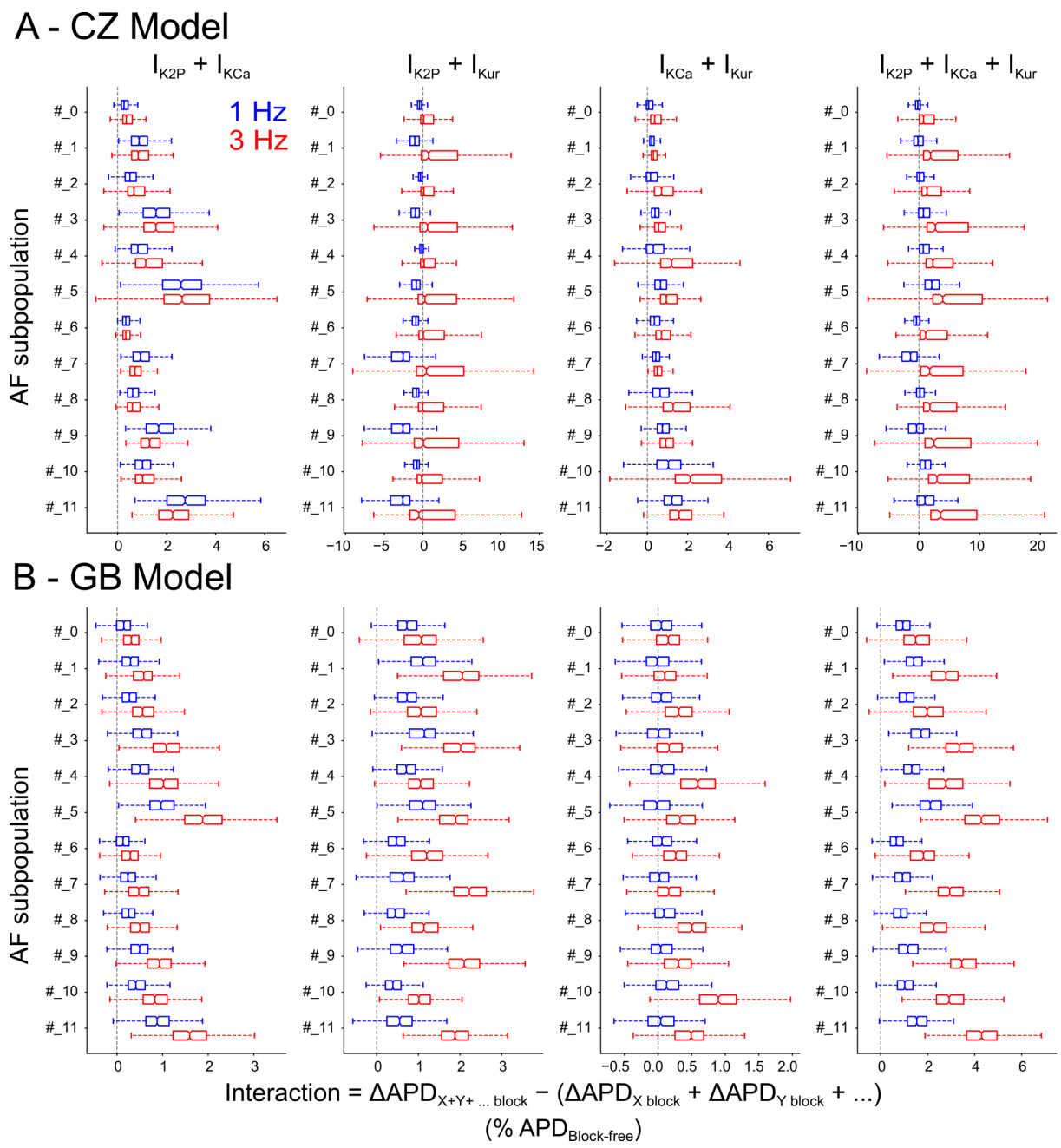

Supporting Figure S5. Boxplot of interactions among multi-current block in APD modulation for cells in each subpopulation.
The interactions were defined as the difference in ΔAPD for the combined effects vs the additive sum of the separate effects and normalized to the cell-matched block-free APD. In these simulations, each current was subjected to 50% block. Positive interaction indicates synergism whereas negative difference suggests antagonism. Data of 1 Hz are shown in blue and 3 Hz in red.

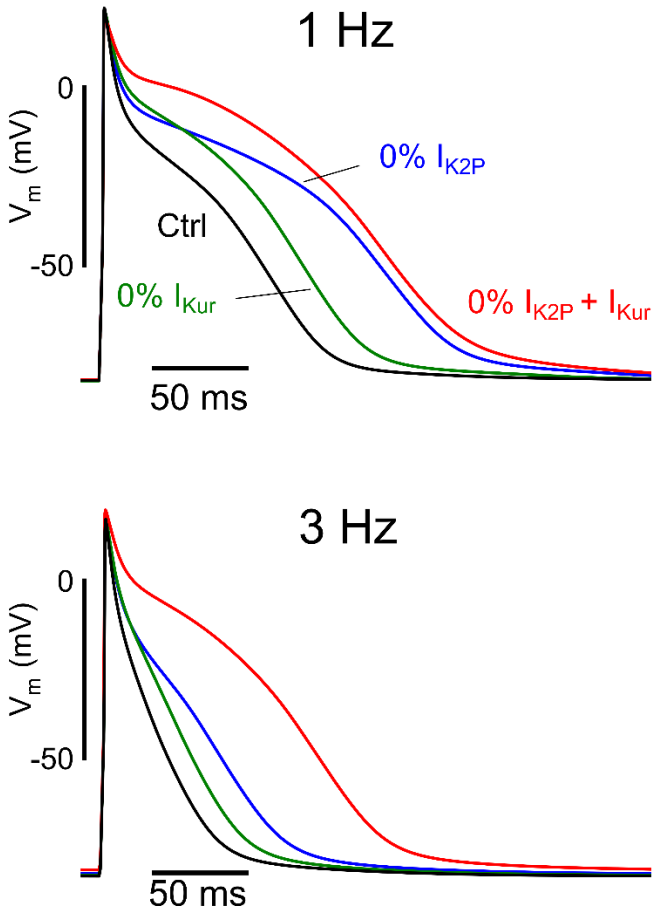

Supporting Figure S6. Example of AP traces showing antagonism in prolonging APD at 1 Hz but synergism at 3 Hz following 100% block of I_{K2P} and I_{Kur} with CZ model (subpopulation #5, variant #383).

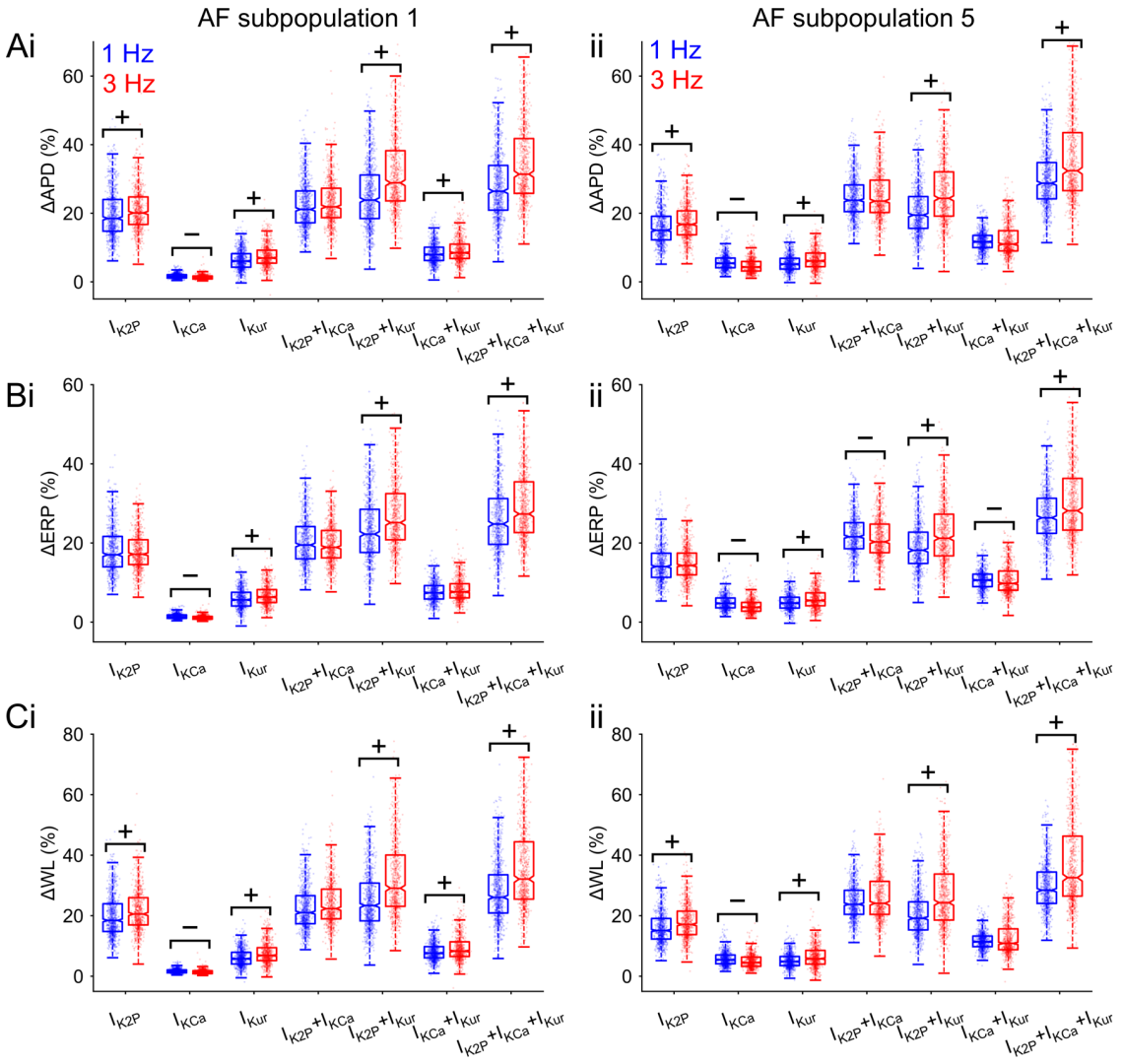

Supporting Figure S7. Effects of mono-K^+ or multi-K^+-current block on virtual atrial tissue populations considering 40% cell-to-cell decoupling. Each row depict change in (A) APD, (B) ERP and (C) WL due to current block obtained from virtual atrial strand populations paced at 1 Hz (blue) and 3 Hz (red). Columns describe results from (i) AF subpopulation #1 and (ii) AF subpopulation #5, respectively. WL was computed as the product of APD and CV. RD was deemed from analysis of CI in difference between 3 Hz vs 1 Hz group: "+" for positive RD and "– " for negative RD.

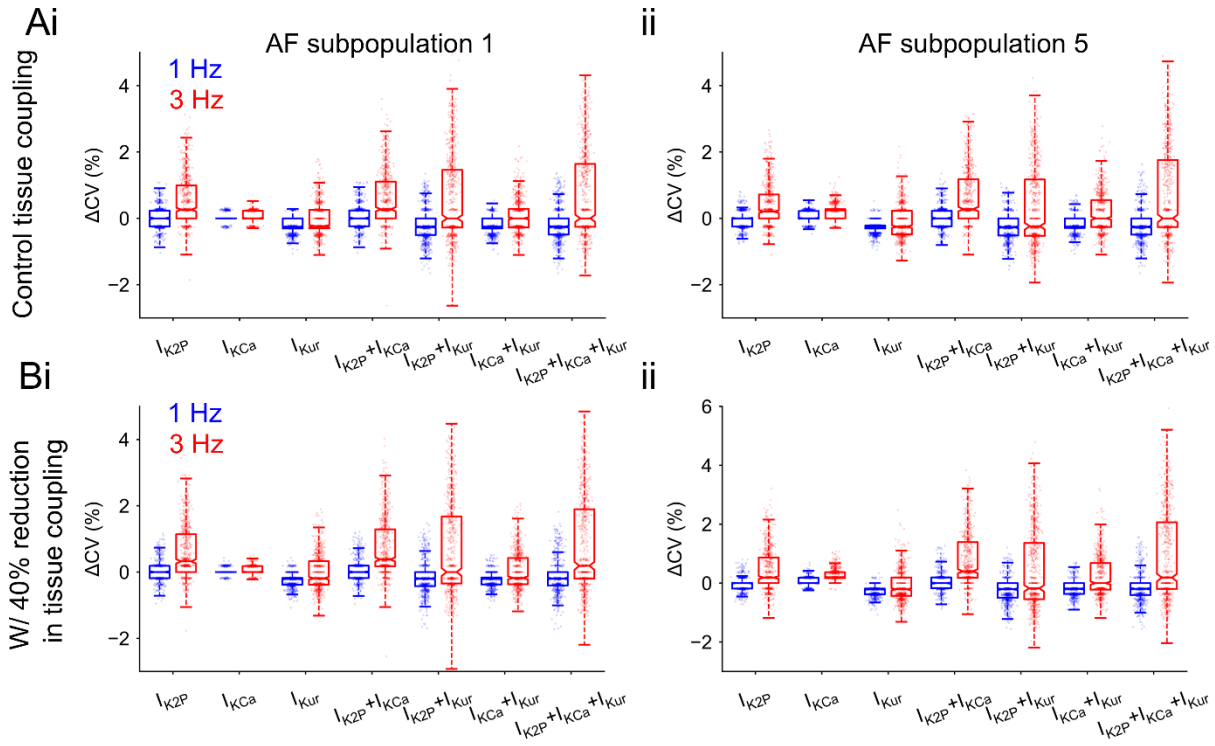

Supporting Figure S8. **Effects of mono- or multi-K^+ current block on conduction velocity from 1D strand models of AF-remodeled atrial tissue paced at 1 Hz (blue) and 3 Hz (red) compared to baseline conditions.** (A-B) Simulations results from virtual atrial tissue with (A) control and (B) 40% reduction of cell-to-cell coupling. Left and right columns describe results from (i) AF subpopulation 1 and (ii) AF subpopulation 5, respectively.

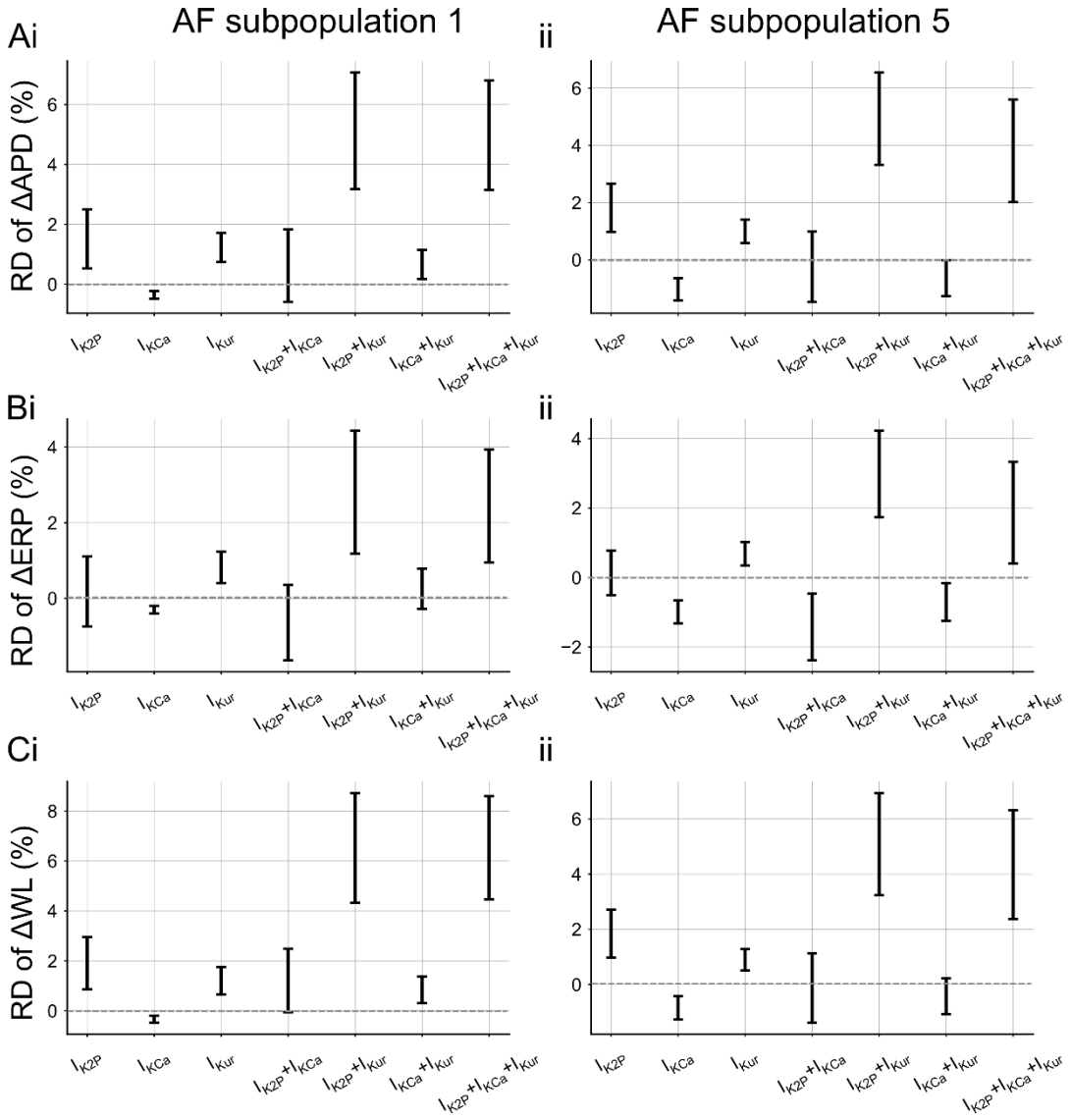

Supporting Figure S9. **Confidence interval analysis of rate-dependent changes in ΔAPD, ΔERP and ΔWL (3 Hz vs 1 Hz) shown in Figure 8 of the main text.**

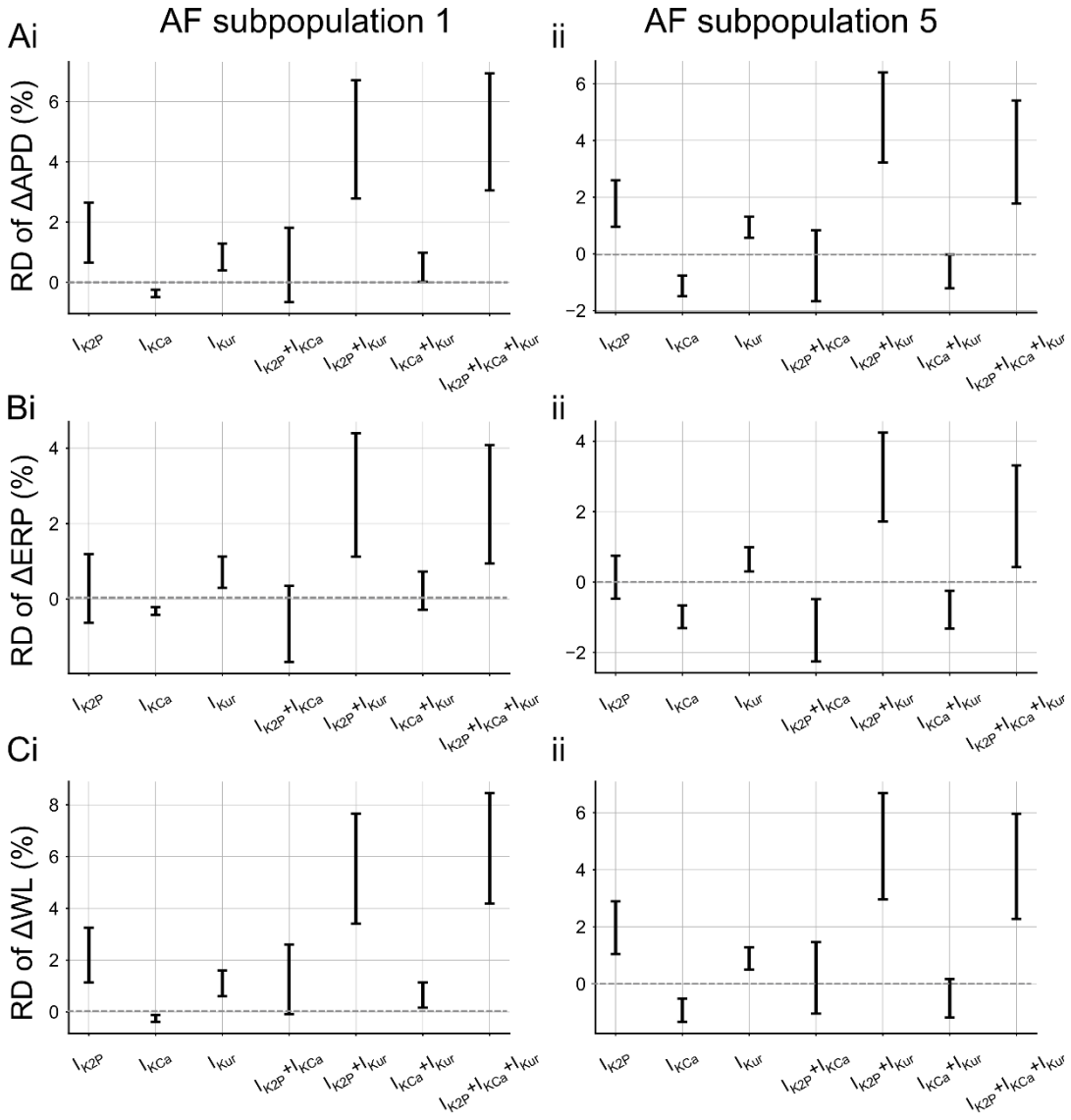

Supporting Figure S10. Confidence interval analysis of rate-dependent changes in ΔAPD, ΔERP and ΔWL (3 Hz vs 1 Hz) with 40% cell-to-cell decoupling shown in Supporting Figure S7.

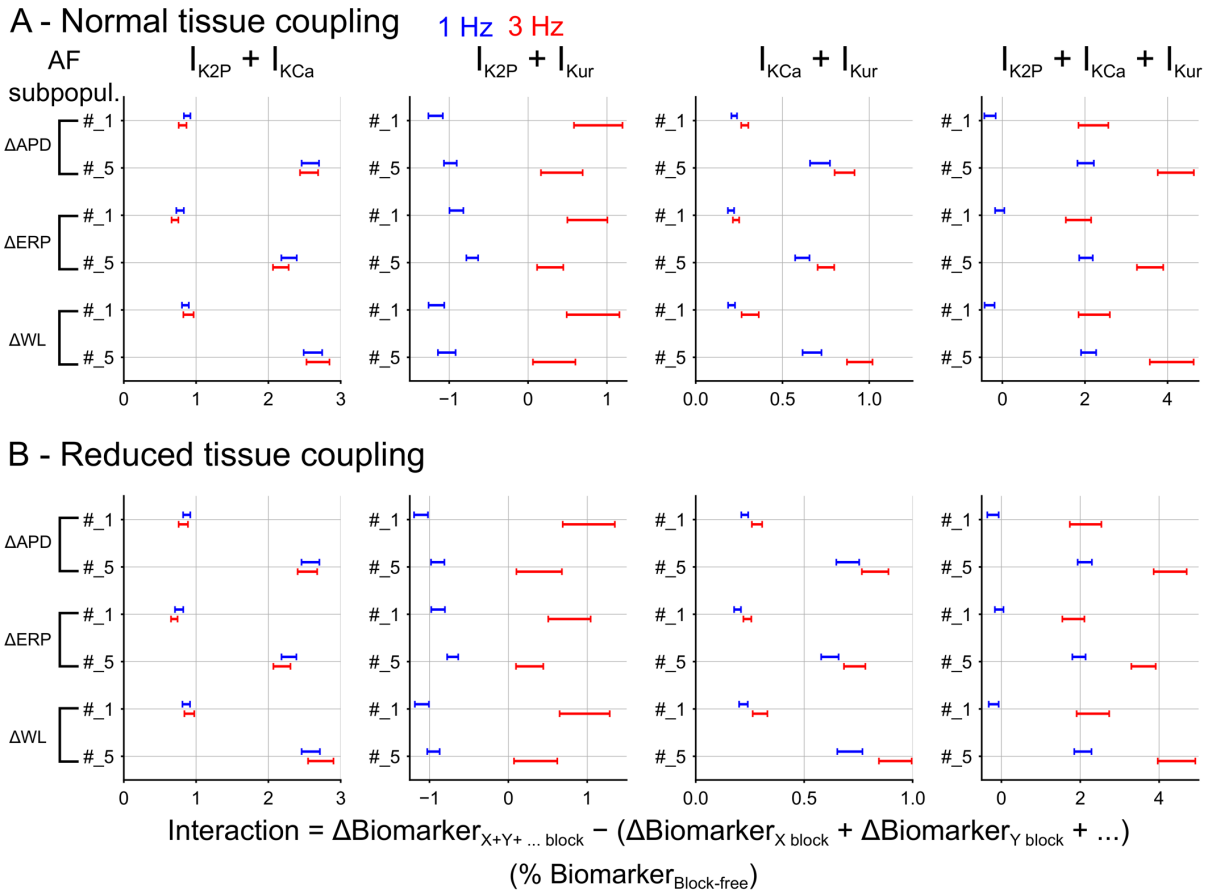

Supporting Figure S11. Analysis of interactions among I_{K2P}, I_{KCa} and I_{Kur} blockade in modulating APD, ERP and WL in tissue simulations.
Confidence intervals were computed for the median interactions in multi-current block defined as the difference in ΔAPD, ΔERP or ΔWL for the combined effects vs the additive sum of the separate effects. Values were normalized to cell-matched block-free values. In these simulations, each current was subjected to 50% block. Positive interaction indicates synergism whereas negative difference suggests antagonism. Data of 1 Hz are shown in blue and 3 Hz in red.

References

Bosch, R.F., Zeng, X., Grammer, J.B., Popovic, K., Mewis, C., and Kühlkamp, V. (1999). Ionic mechanisms of electrical remodeling in human atrial fibrillation. Cardiovasc. Res. *44*: 121–131.

Caballero, R., Fuente, M.G. de la, Gómez, R., Barana, A., Amorós, I., Dolz-Gaitón, P., et al. (2010). In Humans, Chronic Atrial Fibrillation Decreases the Transient Outward Current and Ultrarapid Component of the Delayed Rectifier Current Differentially on Each Atria and Increases the Slow Component of the Delayed Rectifier Current in Both. J. Am. Coll. Cardiol. *55*: 2346–2354.

Canty, A., and Ripley, B.D. (2019). boot: Bootstrap R (S-Plus) Functions.

Colman, M.A., Ni, H., Liang, B., Schmitt, N., and Zhang, H. (2017). In silico assessment of genetic variation in KCNA5 reveals multiple mechanisms of human atrial arrhythmogenesis. PLOS Comput. Biol. *13*: e1005587.

Courtemanche, M., Ramirez, R.J., and Nattel, S. (1998). Ionic mechanisms underlying human atrial action potential properties: insights from a mathematical model. Am. J. Physiol. - Heart Circ. Physiol. *275*: H301–H321.

Cummins, M.A., Dalal, P.J., Bugana, M., Severi, S., and Sobie, E.A. (2014). Comprehensive Analyses of Ventricular Myocyte Models Identify Targets Exhibiting Favorable Rate Dependence. PLoS Comput Biol *10*: e1003543.

Davison, A.C., and Hinkley, D.V. (1997). Bootstrap Methods and Their Applications (Cambridge: Cambridge University Press).

Ellinwood, N., Dobrev, D., Morotti, S., and Grandi, E. (2017a). In Silico Assessment of Efficacy and Safety of IKur Inhibitors in Chronic Atrial Fibrillation: Role of Kinetics and State-Dependence of Drug Binding. Front. Pharmacol. *8*: 799.

Ellinwood, N., Dobrev, D., Morotti, S., and Grandi, E. (2017b). Revealing kinetics and state-dependent binding properties of IKur-targeting drugs that maximize atrial fibrillation selectivity. Chaos Interdiscip. J. Nonlinear Sci. *27*: 093918.

Gonzalez de la Fuente, M., Barana, A., Gomez, R., Amoros, I., Dolz-Gaiton, P., Sacristan, S., et al. (2012). Chronic atrial fibrillation up-regulates 1-Adrenoceptors affecting repolarizing currents and action potential duration. Cardiovasc. Res. *97*: 379–388.

Grammer, J.B., Bosch, R.F., Kühlkamp, V., and Seipel, L. (2000). Molecular Remodeling of Kv4.3 Potassium Channels in Human Atrial Fibrillation. J. Cardiovasc. Electrophysiol. *11*: 626–633.

Grandi, E., Pandit, S.V., Voigt, N., Workman, A.J., Dobrev, D., Jalife, J., et al. (2011). Human atrial action potential and Ca2+ model sinus rhythm and chronic atrial fibrillation. Circ. Res. *109*: 1055–1066.

Morotti, S., and Grandi, E. (2017). Logistic regression analysis of populations of electrophysiological models to assess proarrythmic risk. MethodsX *4*: 25–34.

Morotti, S., McCulloch, A.D., Bers, D.M., Edwards, A.G., and Grandi, E. (2016). Atrial-selective targeting of arrhythmogenic phase-3 early afterdepolarizations in human myocytes. J. Mol. Cell. Cardiol. *96*: 63–71.

Ni, H., Whittaker, D.G., Wang, W., Giles, W.R., Narayan, S.M., and Zhang, H. (2017). Synergistic Anti-arrhythmic Effects in Human Atria with Combined Use of Sodium Blockers and Acacetin. Front. Physiol. *8*: 946.

Ozgen, N., Dun, W., Sosunov, E., Anyukhovsky, E., Hirose, M., Duffy, H., et al. (2007). Early electrical remodeling in rabbit pulmonary vein results from trafficking of intracellular SK2 channels to membrane sites. Cardiovasc. Res. *75*: 758–769.

Peng, R.D. (2019). simpleboot: Simple Bootstrap Routines.

Qi, X.-Y., Diness, J.G., Brundel, B.J.J.M., Zhou, X.-B., Naud, P., Wu, C.-T., et al. (2014). Role of small-conductance calcium-activated potassium channels in atrial electrophysiology and fibrillation in the dog. Circulation *129*: 430–440.

R Core Team (2019). R: A Language and Environment for Statistical Computing (Vienna, Austria: R Foundation for Statistical Computing).

Rush, S., and Larsen, H. (1978). A practical algorithm for solving dynamic membrane equations. IEEE Trans. Biomed. Eng. *BME-25*: 389–392.

Sarkar, A.X., and Sobie, E.A. (2011). Quantification of repolarization reserve to understand inter-patient variability in the response to pro-arrhythmic drugs: a computational analysis. Heart Rhythm Off. J. Heart Rhythm Soc. *8*: 1749–1755.

Schmidt, C., Wiedmann, F., Voigt, N., Zhou, X.-B., Heijman, J., Lang, S., et al. (2015). Upregulation of K2P3.1 K+ Current Causes Action Potential Shortening in Patients With Chronic Atrial Fibrillation. Circulation *132*: 82–92.

Schmidt, C., Wiedmann, F., Zhou, X.-B., Heijman, J., Voigt, N., Ratte, A., et al. (2017). Inverse remodelling of K2P3.1 K+ channel expression and action potential duration in left ventricular dysfunction and atrial fibrillation: implications for patient-specific antiarrhythmic drug therapy. Eur. Heart J. *38*: 1764–1774.

Skibsbye, L., Poulet, C., Diness, J.G., Bentzen, B.H., Yuan, L., Kappert, U., et al. (2014). Small-conductance calcium-activated potassium (SK) channels contribute to action potential repolarization in human atria. Cardiovasc. Res. *103*: 156–167.

Sobie, E.A. (2009). Parameter Sensitivity Analysis in Electrophysiological Models Using Multivariable Regression. Biophys. J. *96*: 1264–1274.

Sundnes, J., Lines, G.T., and Tveito, A. (2005). An operator splitting method for solving the bidomain equations coupled to a volume conductor model for the torso. Math. Biosci. *194*: 233–248.

Wagoner, D.R.V., Pond, A.L., McCarthy, P.M., Trimmer, J.S., and Nerbonne, J.M. (1997). Outward K+ Current Densities and Kv1.5 Expression Are Reduced in Chronic Human Atrial Fibrillation. Circ. Res. *80*: 772–781.

Workman, A.J., Kane, K.A., and Rankin, A.C. (2001). The contribution of ionic currents to changes in refractoriness of human atrial myocytes associated with chronic atrial fibrillation. Cardiovasc. Res. *52*: 226–235.